

---

# Ultra-high Dynamic Range Measurement of High-Contrast Pulses Using a Second-Order Autocorrelator

In high-intensity, ultrafast laser–plasma interactions with solid targets, the intensity of prepulses with a typical time duration of  $\sim 1$  ns, arriving before the main laser pulse, must be less than  $\sim 10^{10}$  W/cm<sup>2</sup> to avoid having the high-intensity pulse interact with a preformed plasma.<sup>1,2</sup> Currently, the highest available peak laser intensities are  $\sim 5 \times 10^{19}$  W/cm<sup>2</sup> with 30-fs pulses<sup>3</sup> for small-scale laboratory lasers and  $10^{21}$  W/cm<sup>2</sup> with 500-fs pulses on a large-laboratory scale.<sup>4</sup> The development of optical parametric chirped-pulse amplification<sup>5</sup> may allow the construction of small-laboratory-scale, truly tabletop subpetawatt lasers with peak intensities in the range of  $10^{21}$  to  $10^{23}$  W/cm<sup>2</sup>;<sup>6</sup> therefore, the dynamic range of temporal pulse measurements must exceed  $\sim 10^{12}$  to predict if, where, and when a preformed plasma will be produced. Detailed knowledge of the temporal shape of the pulse is crucial to the study of high-density plasma physics.<sup>7</sup> The interaction of a high-contrast pulse with a high-density solid target or a high-density plasma is completely different from that of a low-contrast pulse. In particular, efficient production of the ultrafast x-ray emission<sup>8,9</sup> may require a high-contrast pulse.<sup>10</sup>

In some cases the intense pulse will contain a long, low-contrast prepulse with known temporal shape. The temporal shape of this prepulse must be known since it will affect the outcome of the interaction. At  $10^{21}$  W/cm<sup>2</sup> intensities, a prepulse at the level of  $\sim 10^{-12}$  below peak intensity produces a preformed plasma, while one at the 0.1% level of peak intensity can ionize atoms and ponderomotively accelerate electrons out of the focus before the main pulse arrives. A pulse of this kind is used in the fast ignitor,<sup>11</sup> where a long, low-contrast ( $\sim 10^{-3}$  below peak intensity) prepulse bores a hole for the main pulse. The temporal history of the prepulse will critically affect the propagation of the intense laser pulse in a large-scale coronal plasma and the energy deposition process in the overdense region.

With current state-of-the-art, ultrashort, high-peak-intensity lasers, the ideal device for measuring the temporal profile of the pulse would be a device with temporal resolution of tens of femtoseconds and a dynamic range of  $10^{12}$ .

Devices simultaneously possessing subpicosecond resolution and high dynamic detection range are noncollinear beam correlators based on frequency conversion. The pulse to be measured is split into two parts, one of which may be delayed by the time delay  $\tau$ , attenuated, and perhaps modified in frequency. The two parts are recombined in a nonlinear medium. In high-dynamic-range autocorrelation (HDRA), the sum frequency is generated noncollinearly to avoid the direct exposure of the detector by each individual beam. In second-order (SO) HDRA, where the noncollinearly recombined replicas of the beam are identical, the second-harmonic energy  $E_{2\omega}(\tau)$  as a function of delay is proportional to the second-order intensity correlation function<sup>12</sup> (autocorrelation function):

$$E_{2\omega}(\tau) \propto G^{(2)}(\tau) \propto \int I(t)I(t-\tau)dt,$$

where  $I(t)$  is the intensity.

In third-order (TO) HDRA, one beam is frequency doubled before noncollinear recombination, and the resulting third-harmonic signal  $E_{3\omega}(\tau)$  is proportional to the third-order intensity correlation function<sup>13</sup>

$$E_{3\omega}(\tau) \propto G^{(3)}(\tau) \propto \int I(t)I^2(t-\tau)dt.$$

The advantages of SO over TO HDRA are simplicity, longer wavelength of the recorded signal, and better temporal resolution. Deteriorated temporal resolution in TO HDRA can be due to the limited acceptance bandwidth of the tripler<sup>14,15</sup> and, for shorter pulses ( $\sim 100$  fs and shorter), due to the dispersion of the pulse in the doubler or relay optics of autocorrelator.<sup>3,15</sup> The main advantage of TO over SO HDRA is that it can distinguish prepulses from postpulses.

The required proportionality of  $E_{2\omega}(\tau)$  on the square of the incident intensity,  $E_{2\omega}(\tau=0) \propto (I_{\omega})^2$ , is satisfied over many orders of magnitude of incident intensities, so no

modification in the optical part of the autocorrelator or in the attenuation of the input beam is required when the delay  $\tau$  is increased. A square-law, slow detector (with nanosecond resolution) is usually attenuated with calibrated filters to keep the noncollinear, sum-frequency signal at approximately the same level. In addition, the detected signal can be electronically time gated (on a time scale of  $\sim 10$  ns) to minimize any extraneous noise associated with long-time-scale optical or electrical background.

Ultrafast pin diodes or streak cameras possess neither the required temporal resolution nor the required high dynamic range. The typical dynamic range of a streak camera with picosecond resolution is 100. It can be boosted to  $10^7$  by nonlinear shutters, by operating at lower temporal resolutions, and, for stable laser systems, by averaging over many laser shots.<sup>16</sup> The main disadvantage of correlators is that they are an indirect method of detection, i.e., the transformation of the signal from  $I(t)$  to  $G^{(2)}(\tau)$  occurs nonlinearly, allowing the existence of multiple solutions during reconstruction of the primary signal from the correlation signal. Both streak cameras and autocorrelators lose important temporal-phase information of the pulse. Recently, several methods have been developed to completely characterize ultrashort pulses, i.e., to obtain the temporal-phase and intensity information about the most intense portion of the beam. This is done with autocorrelators that frequency resolve the autocorrelation signal. The single-shot technique, which is able to completely characterize the most intense portion of the pulse, such as frequency-resolved optical gating (FROG),<sup>17</sup> is well developed with SO and TO noncollinear autocorrelators. These techniques, however, have not demonstrated a dynamic range approaching  $10^{12}$ .

For ultrashort intense pulses, it is necessary to perform additional high-contrast autocorrelation to obtain information about the temporal-energy distribution outside the most intense portion. In this article, we perform only high-contrast autocorrelation measurements, although the autocorrelator used is “FROG-ready” and can work in the single-shot regime if the on-crystal focusing lenses are removed. The phase-sensitive measurements were not performed because the measured pulse was close to its bandwidth limit.

### Noncollinear Autocorrelator for Temporal-Pulse-Shape Measurements

The  $z$  coordinate (transverse) of the spatial profile of the wide second-harmonic (SH) beam<sup>18,19</sup> or third-harmonic beam<sup>15</sup> may be linearly mapped to the delay  $\tau$  to obtain the

corresponding autocorrelation function in a single shot, as shown on Fig. 75.8. Figure 75.8 illustrates type-I noncollinear phase matching for two wide beams of diameter  $D$ , represented by ordinary waves with carrier frequency  $\omega$ , ( $o, \omega$ ) propagating in a doubling crystal with thickness  $L_c$  at angle  $\Phi$  with respect to each other. The direction of the noncollinearly generated second-harmonic extraordinary ( $e, 2\omega$ ) beam is determined by the phase-matching condition,  $\vec{k}_{o_1, \omega} + \vec{k}_{o_2, \omega} = \vec{k}_{e, 2\omega}$ . To maintain the correspondence between the transverse signal profile  $S_{2\omega}(z)$  and the autocorrelation function  $G^{(2)}(\tau)$  over the most intense temporal portion of the pulse, the transverse sizes ( $D$ ) of the interacting beams should be large to avoid distorting the shape of the SH beam due to the spatial shape of the fundamental beam. The following two conditions should be satisfied: the spatial walk-off of each beam along the  $z$  coordinate in the thickness of the crystal,  $L_c \tan(\Phi/2)$ , should be at least three times smaller than the beam diameter size along the  $z$  direction,  $D \cos(\Phi/2)$ , giving  $L_c \tan(\Phi/2) \leq (D/3) \cos(\Phi/2)$ , and the size of the interaction region (diamond-shaped region in Fig. 75.8) should be at least three times smaller than the transverse size of the beam  $D$ , giving  $L_p / \tan(\Phi/2) \leq D/3$ .  $L_p \approx (c/n_{o, \omega}) \tau_p$  is the physical length of the pulse inside the crystal,  $c$  is the speed of light,  $n_{o, \omega}$  is the index of refraction, and

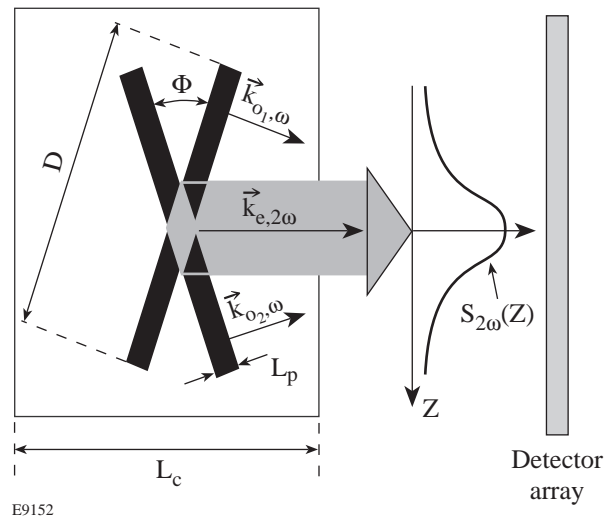


Figure 75.8

Single-shot setup for the noncollinear second-order autocorrelator. Two wide, ordinary beams with  $k$ -vectors  $\vec{k}_{o_1, \omega}$  and  $\vec{k}_{o_2, \omega}$ , propagating in the nonlinear crystal at angle  $\Phi$  with respect to each other, create a second-harmonic beam  $\vec{k}_{e, 2\omega}$ . The width of the generated second-harmonic beam depends only on the duration of the pulses if beam diameters  $D$  are large. The shape of the second-harmonic beam, which is proportional to the second-order autocorrelation function  $G^{(2)}(\tau)$ , is recorded with a linear detector array.

$\tau_p$  is the pulse duration. The single-shot setup is limited to an  $\sim 10$ - to 100-ps range of delays ( $\tau$ ), due to the finite sizes of the crossing beams and/or the nonlinear crystal,<sup>14</sup> and to a dynamic range of  $\sim 10^6$  to  $10^7$ .<sup>15,20</sup> The finite dynamic range is due to the scattering of the intense portions of the noncollinearly generated beam into low-intensity portions.

To obtain a higher dynamic range with a delay of hundreds of picoseconds, one must work in the scanning regime when only one point of autocorrelation function (one  $\tau$ ) is recorded during a single shot. This is shown in Fig. 75.9, where the linear detector array is replaced by a single-point detector. In an experiment, the averaged autocorrelation function

$$\bar{G}(\tau, \Delta\tau) = \frac{1}{\Delta\tau} \int_{\tau-\Delta\tau/2}^{\tau+\Delta\tau/2} G(\tau') d\tau'$$

is recorded, instead of  $G(\tau)$ , due to finite sizes of the crossing beams. To avoid the effect of averaging  $\bar{G}(\tau) = G(\tau)$ , the transverse beam sizes at the intersection point inside the crystal must be reduced to one-third of the beam size obtained in a single-shot setup, or the time window determined by the crossing beams must be less than approximately one-tenth of

the pulse duration  $\Delta\tau \lesssim \tau_p/10$ . Figure 75.9 can be compared to Fig. 75.8. In Fig. 75.9, the beam diameters are reduced by a factor of 10, and, consequently, the  $z$  width of the SH beam is reduced by factor of 3 with respect to the original single-shot size. The transverse size  $D = 2w_0$  of the crossing beams should satisfy  $D/\{L_p/\sin(\Phi/2)\} \lesssim 0.3$ . The sizes of the beams and their crossing angle will define the temporal resolution

$$\Delta\tau \approx (1.2/\gamma)(Dn_{o,\omega}/c)\tan(\Phi/2), \quad (1)$$

where  $\gamma$  is the form factor relating the FWHM of  $I(t)$  to that of  $G^{(2)}(\tau)$ .

For  $\sim 100$ -fs and shorter pulses, dispersion may be a factor in the temporal resolution, or more correctly, dispersion will affect the width of the measured autocorrelation function because the lengths of interacting pulses,  $L_p$ , will be different upon arrival at the interaction point.

In the case of the finite transverse width of the probe pulse and negligible dispersion, the recorded autocorrelation function is proportional to the pulse shape  $G(t) \propto I_\omega(t)$  at all times where  $I_\omega(t)$  changes slowly, i.e., far from the most intense

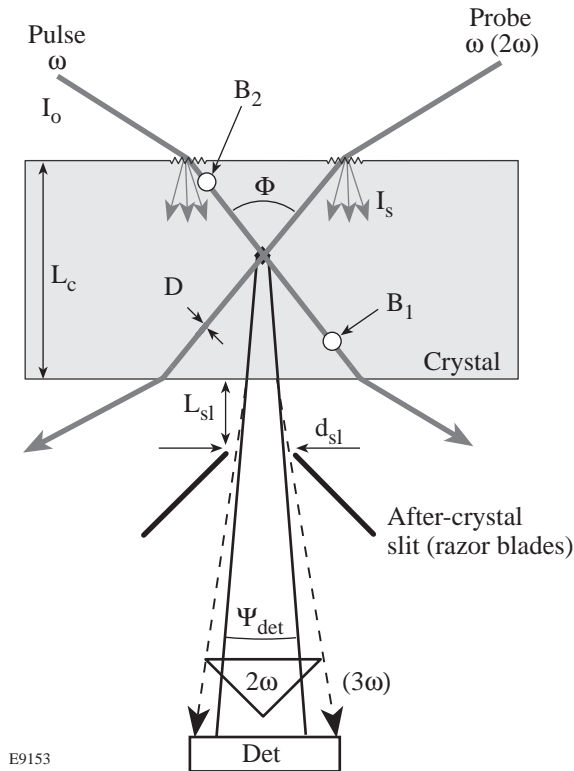


Figure 75.9

Geometry of the crossing beams in a noncollinear scanning autocorrelator. Two focused beams cross inside the crystal and generate the sum-frequency signal noncollinearly. For a particular delay between the pulse and the probe beams, the energy generated in the interaction region is proportional to the autocorrelation function. This geometry gives only one point of the auto-correlation function for a particular delay between the two beams (scanning regime) but allows one to obtain the higher dynamic range required for measurements of intense, ultrashort pulses. The light scattered from the first surface  $I_s$  (shown with arrows originating from the rough surface) can be frequency doubled during propagation through the bulk of the crystal and can reach the detector. An after-crystal slit is installed to reduce it. Each individual beam can be frequency converted along the passage through the crystal and then can scatter into the direction of the detector, producing a delay-independent background. We assume that only some portion of the beam path between points  $B_1$  and  $B_2$  is visible from the detector due to the presence of the after-crystal slit. We refer to this type of background as bulk-scattering noise.

region. The most intense portion is modified due to the autocorrelation transformation [integration of  $I(t)I(t-\tau)$ ]. For example, for the temporal Gaussian/sech<sup>2</sup> pulse shape of  $I(t)$  with a symmetric low-intensity pedestal, the  $G^{(2)}(\tau)$  is 1.4 to 1.5 times wider than  $I(t)$  and gives a pedestal intensity that is overestimated by factor of 2.8 to 3.

In several previous works, authors have measured 0.1- to 1-ps pulses with SO HDRA<sup>21–25</sup> with dynamic ranges of  $10^5$  to  $10^8$  and with TO HDRA<sup>26–31</sup> with dynamic ranges of  $10^6$  to  $10^8$ . In two works,<sup>3,13</sup> the dynamic range with a TO autocorrelator is up to  $10^{10}$  for 10-ps and 30-fs pulses with a temporal resolution of  $\sim 1$  ps and  $\sim 0.1$  ps, respectively (affected by dispersion). In the latter reference, the recorded autocorrelation function does not follow  $G^{(3)}(\tau)$  over the most intense portion of the pulse, and additional second-order, single-shot, low-contrast autocorrelation is performed to complement the high-contrast measurements. In all of the cited references, there were no estimates of the factors that limit the available dynamic range.

In modern short-pulse laser systems, a contrast measurement of  $10^8$  may be insufficient. In a conventional CPA laser system, where a nanojoule-level oscillator determines the high-dynamic-range structure of the pulse, the contrast of optical background is  $\sim 10^8$  or lower.<sup>32–35</sup> This optical background usually propagates through the CPA system and is present in the final amplified and compressed pulse. In addition, after stretching and relay losses, the amplified pulse may acquire a background associated with the amplified spontaneous emission (ASE) of the amplifier itself. As a rule of thumb, the contrast of the compressed pulse resulting from ASE noise of an amplifier can be expressed as the number of injected photons within the gain-narrowed spectrum, if the injected-pulse spectrum is wider than the gain-narrowed spectrum supported by this amplifier. Typically, with a pulse energy of  $\sim 100$  pJ injected into the first regenerative or multipass amplifier, the ASE background may be of the order of  $10^{-8}$  below the peak intensity in the compressed pulse.

In the case of insufficient pulse contrast, several schemes have been proposed to increase it. These include the use of the nonlinear birefringence of the fibers,<sup>32</sup> Pockels cells,<sup>20</sup> saturable absorbers,<sup>21</sup> frequency doubling of the amplified pulse,<sup>36,37</sup> degenerate optical parametric amplification (OPA),<sup>38</sup> amplification based on stimulated Raman scattering,<sup>39</sup> and self-induced plasma shuttering.<sup>23</sup> Using feedback-controlled mode-locked (FCM) lasers<sup>40</sup> with a saturable absorber inside the cavity makes it possible to create 1-ps pulses with  $\sim 10^8$

contrast and  $\sim 1$ - $\mu$ J energy,<sup>27</sup> which effectively nullifies the influence of ASE of subsequent amplifiers to the level of  $10^{-12}$ . For OPA CPA,<sup>5</sup> where co-propagating amplified and pumped pulses are timed and matched in duration, the long-duration ASE noise does not exist, due to the absence of an inverted medium. In many of the above-mentioned, experimentally realized schemes, the estimated contrast of picosecond and shorter pulses may be higher than  $10^{12}$  but has not been measured.<sup>36–39</sup>

We have analyzed the factors that limit the dynamic range of the noncollinear autocorrelators and have systematically minimized them. The main physical factors are the finite energy of the pulse, scattering from the surface of the crystal, and bulk scattering. Minimizing or eliminating noise resulting from these factors dictates the geometry of the crossing beams in the autocorrelator and the size and quality of the crystal for a given pulse duration. Our estimate for the dynamic range is carried out for SO HDRA but can be applied to TO HDRA as well because both use the second-order nonlinearity  $\chi^{(2)}$  of the medium [a cascaded  $\chi^{(2)}:\chi^{(2)}$  process in the case of TO autocorrelation measurements] to produce the noncollinear signal.

The dynamic range of the autocorrelator can be conveniently defined as the ratio of the noncollinear signal at zero delay ( $\tau=0$ ) to the sum of signals  $E_1$  and  $E_2$  due to each beam, one at a time, sensed by the detector when the other beam is blocked:

$$DR = E_{nc}(\tau=0)/(E_1 + E_2). \quad (2)$$

This definition is independent of the temporal pulse shape and beam delay. Here  $E_{nc}$ ,  $E_1$ , and  $E_2$  are the energies that reach a detector from the noncollinear signal at zero delay and from each individual beam, respectively. It is assumed that  $E_1, E_2 \ll E_{nc}$ , and that the detector is frequency filtered to detect only the sum of the frequencies. The noise signals  $E_1$  and  $E_2$  reaching the detector can be scaled according to the second-harmonic-generation (SHG) equation<sup>41</sup> with additional spatial averaging into the detector:

$$E_{1,2} \propto I_{1,2}(2\omega) \propto \int d_{\text{eff}}^2 L^2 \text{sinc}^2 \left[ \frac{\Delta k(\Omega)L}{2} \right] I_{1,2}^2(\omega, \Omega) d\Omega_{\text{det}}. \quad (3)$$

Here  $\text{sinc}(x) = \sin(x)/x$ ,  $d\Omega_{\text{det}}$  is the solid angle subtended by the detector from a point in the interaction region,  $I(\omega, \Omega)$  is the

fundamental harmonic intensity into the direction of the detector,  $L$  is the interaction length for SHG,  $\Delta k$  is the phase mismatch, and  $d_{\text{eff}}$  is standard shorthand for the effective second-order nonlinearity. Equation (3) assumes that the regions of the surface and of the bulk of the crystal traversed by the beams become weak secondary sources of light at the sum frequency (the frequency of noncollinear signal) due to the scattering followed by frequency conversion or due to the frequency conversion (of strong but SHG phase-mismatched beams) followed by scattering. The highly directional noncollinear (nc) signal is scaled with the same parameters:<sup>18,42</sup>  $E_{\text{nc}} \propto d_{\text{eff,nc}}^2 L_{\text{nc}}^2 I_1 I_2$  (for  $\Delta k = 0$ ).  $L_{\text{nc}}$  can be roughly estimated as the walk-off distance when one beam crosses the other. These equations allow an estimate of the amount of noncollinear signal produced by two beams and the background produced by each individual beam. With the known position of the entrance pupil of the detector and the scattering properties of the crystal, the noncollinear signal can be compared to the signal produced by the scattered light, and the dynamic range of the noncollinear autocorrelator can be estimated.

### Finite Pulse Energy

When the energy of the amplified pulse exceeds several millijoules, the current state-of-the-art lasers can operate only at a low repetition rate—typically 1 to 10 Hz for the first amplification stage and less for the second and higher stages. In this case, a multipulse averaging technique (such as lock-in detection) is impossible. A detector signal corresponding to below 1 photon per pulse in the incident radiation is not practically extractable. If we assume that the equivalent noise level of the device is 10 photons per pulse, to obtain the dynamic range of  $10^{12}$ ,  $10^{13}$  photons, or  $3 \mu\text{J}$  of energy, are required in the second-harmonic noncollinear signal at the peak ( $\tau = 0$ ) for  $1\text{-}\mu\text{m}$  fundamental light. The undepleted second-harmonic signal ( $E_{\text{nc}} \propto I_1 I_2$ ) can be produced with  $\sim 10\%$  efficiency; hence, a  $30\text{-}\mu\text{J}$  pulse is required at the entrance to the crystal. For high-repetition-rate lasers, such as oscillators, lock-in detection can reduce requirements for the energy of individual pulses by 3 or more orders of magnitude. For example, several types of ultrashort-pulse oscillators, with individual-pulse energy in the range of 1 nJ, have been characterized with dynamic ranges of  $10^8$ .<sup>32–35</sup>

### Surface Scattering

Light scatters from a rough surface according to<sup>43</sup>

$$\frac{I_s}{I_0} = \left( \frac{4\pi\delta}{\lambda} \right)^2, \quad (4)$$

where  $I_0$  and  $I_s$  are the incident and scattered intensities,  $\lambda$  is the wavelength of the incident radiation, and  $\delta$  is the rms surface roughness. Equation (4) is valid for near-normal incidence and relatively smooth surfaces,  $\delta \ll \lambda$ . It is assumed that light scatters from the surface isotropically. With typical numbers  $\delta \approx 50 \text{ \AA}$  and  $\lambda = 1 \mu\text{m}$ , we find  $I_s/I_0 = 0.4\%$ , which is very high. The fundamental light scattered from the surface can propagate through the crystal, be frequency doubled, and reach the detector, shown in Fig. 75.9 as arrows originating from the rough surface. The detector is assumed to be blocked against the fundamental light. Using the scaling of Eq. (3) with  $I(\omega, \Omega) = (1/4\pi) I_s$ ,  $d\Omega_{\text{det}} \approx 10^{-2}$  steradians, a mismatch factor  $\text{sinc}^2(\Delta k L_c/2) \approx 10^{-5}$ , and the SHG length of the surface-scattered noise equal to the crystal bulk length  $L_c [L_{\text{scat}} = L_c \sim 1 \text{ mm} (L_{\text{scat}}/L_{\text{nc}} \approx 10)]$ , the signal-to-noise level is approximately  $10^8$ . This is about three to four orders of magnitude lower than required. The scattering in a particular direction can be enhanced if the surface is manufactured with a characteristic roughness period, which acts as a diffraction grating.

To reduce the surface-scattering effects, an aperture or slit can be placed just after the crystal to block the surface-scattered light from entering the detector. We refer to this slit as an “after-crystal” slit (see Fig. 75.9). It is evident that this is more effective at higher crossing angles, with smaller entrance-pupil angles of the detector, and/or with thicker crystals. For the two beams crossing halfway in the bulk of the crystal, the condition for reducing surface-scattering noise can be stated as follows: an observer at the detector should not see regions where the interacting beam hits the surface, or the backward image of the detector entrance-pupil angle onto the first surface of the crystal should be within the “dark area” (see Fig. 75.9),

$$d_{\text{sl}} + \Psi_{\text{det}} (L_{\text{sl}} + L_c/n_{2\omega}^e) < L_c \tan(\Phi/2) - 6w_0/\cos(\Phi_{\text{air}}/2). \quad (5)$$

The left-hand side of Eq. (5) is the size of the backward image of the detector onto the first surface of the crystal with slit size  $d_{\text{sl}}$ , crystal thickness  $L_c$ , and distance from second surface of the detector to the slit,  $L_{\text{sl}}$ . The right-hand side is the size of the “dark area” on the first surface of the crystal where the two beams, with waist size  $w_0$ , separated by the distance  $L_c \tan(\Phi/2)$ , are attenuated to  $10^{-8} I_0$ . This is due to the phase-matching and intensity effects on the conversion efficiency. Equation (5) determines the minimum crossing angle or

thickness of the crystal for efficient surface-noise filtering. It also fixes the optimal linear size of the detector  $\Psi_{\text{det}}$  in the crossing plane. The other dimension of the detector is determined purely by the divergence of the noncollinear SHG beam. To maximize the dynamic range, we must choose  $\Psi_{\text{det}}$  to be approximately equal to the divergence of the noncollinear SH beam, assuming that the detector is in the far field.

The following factors should be considered simultaneously with Eq. (5):

1. The size of the fundamental beams determines the resolution of the autocorrelator, the size of the SHG beam, and the size of the after-crystal slit.
2. The crossing angles are limited by the finite birefringence of the crystal. For example, for  $\lambda = 1 \mu\text{m}$ , the maximum crossing angle for  $\text{LiIO}_3$  and  $\text{BBO}$  is  $39^\circ$ , while for  $\text{KDP}$  it is  $20^\circ$ .
3. The closer the slit is to the crystal, the better. The razor blades are positioned at an angle with respect to each other that minimizes  $L_{\text{sl}}$  while keeping the area of contact of the razor blade with the crystal as small as possible. Another reason for such positioning is to avoid blocking each fundamental beam because backwardly reflected light may give additional background.
4. Smaller waists  $\{w_0 = D/2 \ll 0.3L_p / [2 \sin(\Phi/2)]\}$  are impractical because the SHG conversion efficiency will decrease due to the reduced interaction length. Tighter focusing would require higher intensities to keep the energy of the noncollinear signal at the same level, which could result in damage or saturation of the crystal.

The following example illustrates these constraints. Focusing two identical  $w_0 = 2 \text{ mm}$  beams with  $f = 250 \text{ mm}$  lenses into a noncritically phase-matched  $\text{LiIO}_3$  crystal (maximum possible  $\Phi = 39.5^\circ$ ) with  $L_c = 5 \text{ mm}$  will produce a second-harmonic beam with size  $w_{0,2\omega} \approx 100 \mu\text{m}$  and divergence  $\Psi_{2\omega} \sim 10^{-2} \text{ rad}$ . For  $30\text{-}\mu\text{J}$  total energy of the two beams, with  $d_{\text{eff,nc}} = d_{31} = 4.2 \text{ pm/V}$ ,<sup>44</sup> the estimated conversion efficiency will be  $\sim 10\%$ , giving the required  $\sim 3 \mu\text{J}$  per pulse of the noncollinear signal. The corresponding peak intensity of each fundamental beam will be  $\sim 500 \text{ GW/cm}^2$  for a 1-ps pulse duration. For a crystal–slit separation  $L_{\text{sl}} = 10 \text{ mm}$ , one needs a slit width  $d_{\text{sl}} \approx 400 \mu\text{m}$  to transmit 99% of light and a linear angular size of the detector  $\Psi_{\text{det}} \approx 3\Psi_{2\omega} \approx 3 \times 10^{-2} \text{ rad}$ . The other linear angular size of the detector in the plane perpendicular to the

crossing plane is approximately the same and is determined by the divergence of the SH beam. This gives a  $340\text{-}\mu\text{m}$  size of the backward image of the detector onto the first surface of the crystal and the size of the “dark area” as  $600 \mu\text{m}$ . A 2- to 3-mm-thick crystal is required to efficiently filter the surface-scattering noise. With a low-birefringence crystal such as  $\text{KDP}$  ( $\Phi_{\text{max}} \approx 20^\circ$ ), a 6- to 8-mm-thick noncollinear crystal is required to satisfy Eq. (4) and to filter out the surface-scattering noise. In all previously reported SO HDRA’s utilizing a nonlinear crystal for frequency conversion,<sup>21–25</sup> the dynamic range at the level of  $10^8$  to  $10^9$  was probably limited by surface scattering.

### Bulk Scattering

Bulk scattering is always present in the background and presents the fundamental limitation to the dynamic range of the autocorrelator. Each beam propagating through the crystal can be scattered into the direction of the detector and converted to SH noise or can be converted to the SH and then scattered. The latter process is more probable because the scattering is inversely proportional to the fourth power of wavelength  $R \propto 1/\lambda^4$ .  $R$ , expressed in  $\text{cm}^{-1}\text{sr}^{-1}$ , is the bulk-scattering intensity ratio  $I_s/I_0$  per unit length traveled in the bulk of a solid material per unit solid angle. Bulk scattering depends on the macroscopic index-of-refraction inhomogeneities of a dielectric,  $\Delta n$ ,<sup>45</sup>

$$R = \frac{C}{\lambda^4} (\Delta n)^2, \quad (6)$$

where  $\lambda$  is expressed in  $\mu\text{m}$  and  $C \approx (2 \text{ to } 4) \times 10^3 \mu\text{m}^4 \text{ cm sr}^{-1}$ . The angular and polarization dependence of the scattered light is omitted for the purposes of these estimates. Well-manufactured amorphous glasses have  $\Delta n \approx 10^{-4}\text{--}10^{-5} \text{ cm}^{-1}$  and follow the  $\lambda^{-4}$  laws.<sup>46</sup> Good-quality optical crystals may have  $\Delta n \approx 10^{-6} \text{ cm}^{-1}$  and  $R \approx 10^{-8}$  for visible light. For the smaller bulk-scattering ratios ( $R \leq 10^{-8}\text{--}10^{-9} \text{ cm}^{-1} \text{ sr}^{-1}$ ), the scattering from a single molecule can be comparable to the scattering from macroscopic inhomogeneities.

Here we describe the level of noise scattered into the detector from a single beam converted to the second harmonic and then scattered. We assume that SHG occurs over a 1-mm length along the  $k$ -vectors ( $\vec{k}_{o_1,\omega}$  and  $\vec{k}_{o_2,\omega}$ ) of the beams. This gives the ratio of the bulk-generated to noncollinearly generated intensities:

$$I_{2\omega,\text{bulk}}/I_{2\omega,\text{nc}} = (L_{\text{bulk}}/L_{\text{nc}})^2 \text{ sinc}^2(\Delta k L_{\text{bulk}}/2) \approx 10^{-3}.$$

Taking  $\Delta n \sim 10^{-5} \text{ cm}^{-1}$  gives  $R_0 = 10^{-7}$  for  $\lambda = 0.5 \mu\text{m}$ . The highly fluctuating function  $\text{sinc}^2(x)$  may be replaced on average with  $1/2x^2$ . With the solid angle of the detector  $d\Omega_{\text{det}} \approx 10^{-2}$  steradian, the fraction  $R_0 L_{\text{im}} d\Omega_{\text{det}} \approx 10^{-10}$  of the light will be scattered into the direction of the detector, giving background noise at the level  $10^{-3} \times 10^{-10} = 10^{-13}$ . Here,  $L_{\text{im}} \sim 1 \text{ mm}$  is the length of the path of the single beam inside the crystal, which is visible from the detector as shown in Fig. 75.9 with end points  $B_1$  and  $B_2$  and with  $L_{\text{im}} = |B_1 - B_2|$ . This path segment is the secondary source of SHG noise, which creates delay-independent background into the detector. The non-collinear signal will be  $\sim 5 \times 10^{12}$  times stronger than the bulk-scattering signal.

Here we discuss the bulk-noise level into the detector in the case where the fundamental beam first scatters in the bulk and where the scattered portion is converted into the second harmonic. The portion of the fundamental harmonic scattered into

the direction of the detector from the segment path  $[B_1 B_2]$  is  $(R_0/16) L_{\text{im}} d\Omega_{\text{det}} \approx 10^{-11}$ . The SHG (even perfectly phase matched) is the square of this expression. Even if the SHG length of this scattered beam is an order of magnitude higher than the effective SHG length of the main noncollinear signal, the estimated dynamic range is  $\sim 10^{18}$ , making this scattering process negligible.

Portions of the individual beams directly converted into the second harmonic and then scattered into the direction of the detector limit the dynamic range of the autocorrelator to the level of  $5 \times 10^{12}$  with the refractive bulk inhomogeneities in the 1-mm-thick crystal at the level of  $\Delta n \sim 10^{-5} \text{ cm}^{-1}$ .

### Experimental Setup and Results

The experimental setup is shown in Fig. 75.10. The high-contrast pulse is generated in a chirped-pulse-amplification (CPA) system utilizing a chirping fiber. The system consists of

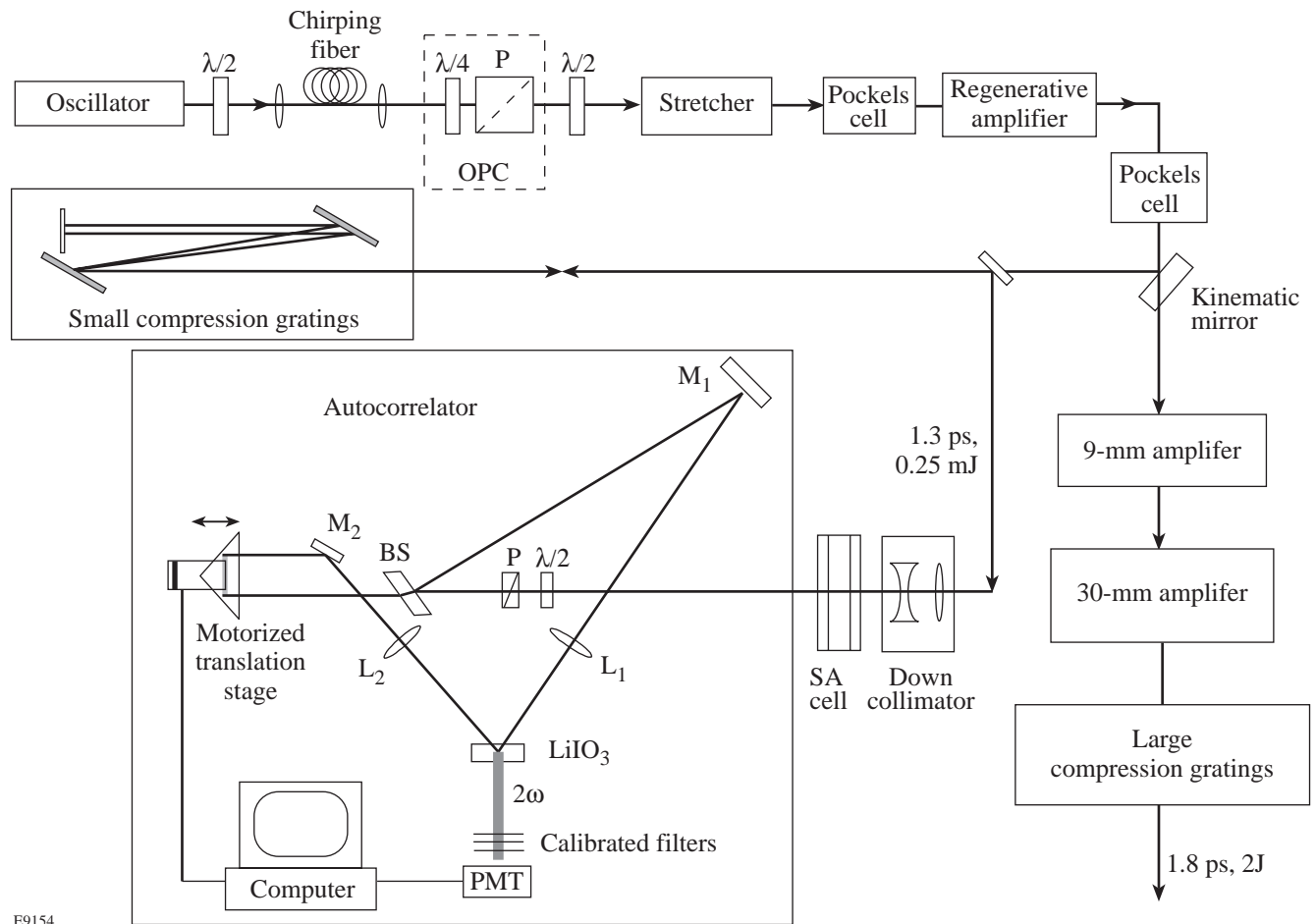


Figure 75.10

Experimental setup for production and measurement of ultrahigh-contrast, 1-ps pulses. OPC: the optical pulse cleaner; P: polarizer;  $\lambda/2$  and  $\lambda/4$ : half- and quarter-wave plates, respectively; BS: beam splitter;  $M_1$  and  $M_2$ : mirrors;  $L_1$  and  $L_2$ : on-crystal focusing lenses; and PMT: photomultiplier tube.

a Nd:YLF oscillator followed by a fiber, a stretcher, three amplification stages, and a grating compressor. The pulse train from the Nd:YLF oscillator<sup>47</sup> is made up of 100-MHz, 45-ps bandwidth-limited pulses at a wavelength of 1053 nm. These pulses pass through an 800-m-long, single-mode optical fiber, which imposes a frequency chirp on the pulse with a bandwidth of up to 40 Å. A grating stretcher is then used to expand the pulse to 450 ps. After the stretcher, one pulse is selected with a Pockels cell for amplification.

The chirped pulse is amplified in three stages. All three amplifiers are flash-lamp-pumped, water-cooled rod amplifiers that have Nd<sup>3+</sup>:glass as an active host. The first stage is a non-cavity-dumped, linear regenerative amplifier,<sup>21,48</sup> which provides most of the gain. It operates at a 1-Hz repetition rate. After about 85 passes, one pulse from the regenerative amplifier train with an output energy of ~0.5 mJ is switched out on the leading edge of the pulse-train envelope. The total cumulative *B*-integral of this pulse is ~0.7. This pulse then passes through a 9-mm-diam rod amplifier where its energy is raised to ~60 mJ. The 9-mm rod amplifier amplifies the pulse in one, two, or three passes. The energy of the pulse can be further boosted by 50 times in the third stage with a single-pass, 30-mm rod amplifier. The amplified pulse is compressed with a pair of compression gratings. The energetic parameters of the CPA system are listed in Table 75.II. When compressed, 1.6-ps pulses can carry energies in excess of 2 J and can be focused onto a target with peak intensities up to 10<sup>19</sup> W/cm<sup>2</sup>.

The amplified compressed pulse exhibits a pedestal consisting of two broad, equal-intensity satellite pulses separated from the main pulse by ~60 ps, as shown in Fig. 75.11, curve (a), with solid circles. The existence of two symmetric satellites was ascertained by performing TO HDRA measurements.<sup>21</sup> Their origin is the overlaid pedestal from the oscillator<sup>13</sup> and uncompensated phase distortions from the

chirping fiber. The satellites and long pedestal can be suppressed by two and one-half orders of magnitude by using optical pulse cleaning (OPC) with the nonlinear birefringence of the chirping fiber.<sup>49,50</sup> A quarter-wave plate and a polarizer are inserted, as in Ref. 51, rather than an additional fiber, as in Ref. 32 (Fig. 75.10). The half-wave plate after the OPC is used to restore the polarization necessary for the grating stretcher. The spectrum leaving the chirping fiber was substantially reshaped, as shown in Fig. 75.12. The original spectrum, leaving the fiber without a quarter-wave plate is shown with a solid line. It has peaks at ±20 Å from the central frequency and two wave-breaking sidelobes<sup>52</sup> at ±30 Å. After rotating the wave plate and polarizer for maximum rejection of low-intensity light and maximum transmission of high-intensity light, the spectrum became centrally peaked with reduced peaks at ±20 Å and completely eliminated side lobes, as shown with the dashed line in Fig. 75.12. The spectral intensity of the amplified spectrum is primarily determined by the gain-narrowing in the regenerative amplifier and is almost independent of the injected spectrum. The pulses with contrast improved by OPC are shown in Fig. 75.11 with open diamonds. The seed energy contained within the shape of gain-narrowed spectrum is ~5 pJ. This imposes an ASE background with contrast ~10<sup>7</sup> when the pulse is compressed, as seen in Fig. 75.11 [curve (b)] for delays  $\tau \geq 130$  ps. This background is very sensitive to the alignment of the seed and can be increased by one or two orders of magnitude by a slight mispointing of the seed pulse. The inset in Fig. 75.11 shows the amplified spectrum (solid curve) corresponding to the autocorrelation data (a) and the spectrum after OPC (dashed curve) corresponding to the autocorrelation data (b). The spectral width of the amplified OPC-modified pulse was 11.5 Å (FWHM), with the shape close to Gaussian. With a form factor  $\gamma=1.4$ , the autocorrelation measurement gives a pulse duration of 1.4 ps and a corresponding time-bandwidth product of 0.44.

Table 75.II: Parameters of the CPA system

	In	Out	Total gain (gain in the active host)	Peak fluence	Output spectrum	<i>B</i> -integral
Oscillator		1 nJ/45 ps		–	0.4 Å	
Fiber	1 nJ	0.3 nJ/150 ps	0.5	–	30 Å	~100
Regenerative amplifier	3 pJ/450 ps	0.5 mJ/150 ps	10 <sup>36</sup>	0.1 J/cm <sup>2</sup>	12 Å	0.7
9-mm amplifier (three passes)	0.3 mJ	60 mJ	400	0.1 J/cm <sup>2</sup>	12 Å	0.2
30-mm amplifier	40 mJ	2 J	50	0.5 J/cm <sup>2</sup>	12 Å	0.6

The contrast of the amplified compressed pulses was further boosted by a fast saturable absorber (SA) cell.<sup>21</sup> The compressed pulse was down-collimated to a waist of 0.7 mm before the SA cell to obtain a peak fluence of 25 mJ/cm<sup>2</sup> with 1.4-ps, 0.25-mJ pulses. The SA was Kodak dye #9860 in nitrobenzene with molar concentrations ( $n_M$ ) varying from 50 to 75  $\mu$ M. The relaxation time of this SA is  $\sim$ 4.2 ps.<sup>53</sup> The thickness of the

cell was 1 cm, with  $\sim$ 12.5-mm wall thicknesses. Within the range of incident fluences between 0.01 and 20 mJ/cm<sup>2</sup>, the incident-fluence-dependent absorption coefficient [ $T = \exp(-\alpha L)$ ], as measured with compressed 1.6-ps pulses, was

$$\alpha = \alpha_0 + \alpha_{\text{sat}} \left[ 1 + (J_{\text{inc}}/J_{\text{sat}})^n \right]^{-1},$$

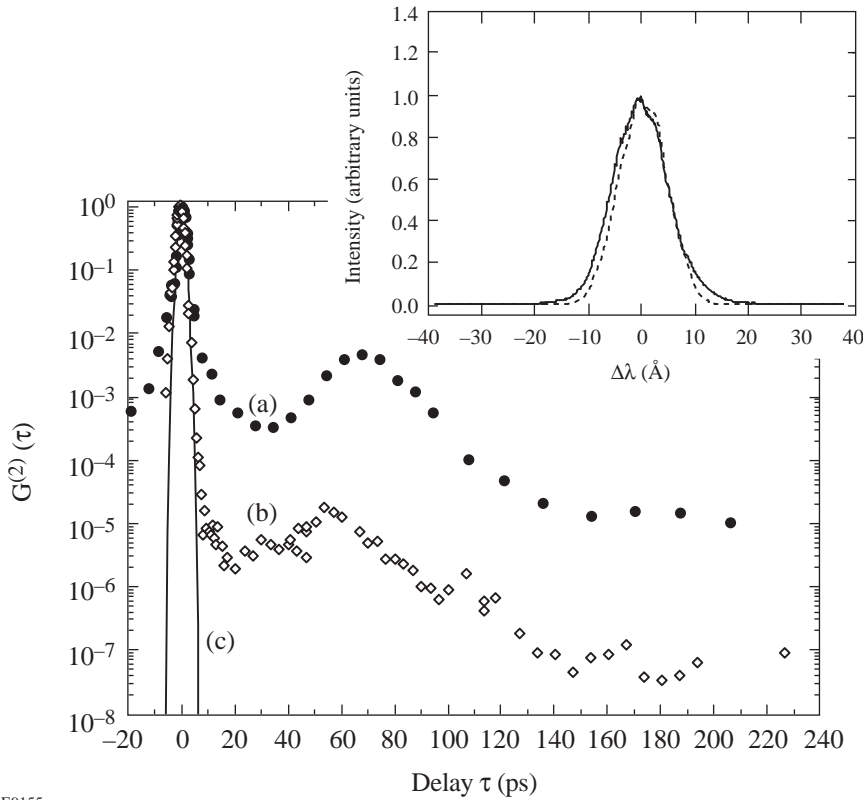


Figure 75.11 Normalized second-order autocorrelation functions of the compressed pulses leaving the regenerative amplifier: (a) original pulses, (b) OPC-cleaned pulses, and (c) the 1.4-ps Gaussian-curve fit to both of these autocorrelation functions. The origin of the pedestal and two symmetric satellites is the oscillator and the uncompensated (after compression with gratings) phase distortions from the chirping fiber. After OPC cleaning and amplification, the pedestal level is determined by the ASE from the regenerative amplifier, which is nearly equal in intensity to the residual pedestal from the oscillator and fiber.

E9155

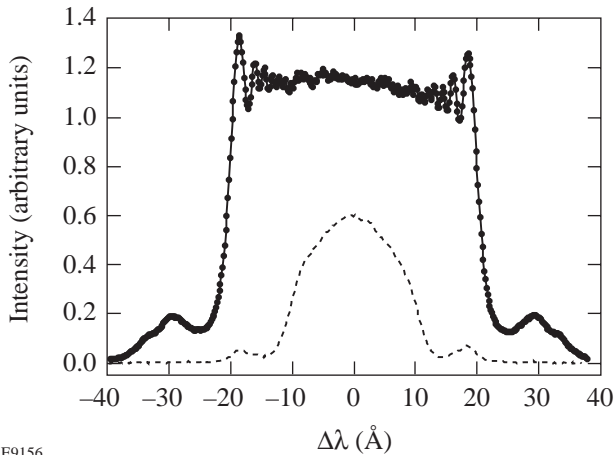


Figure 75.12 The spectrum leaving the chirping fiber. The spectrum measured without a quarter-wave in the OPC is shown with solid line. The OPC-cleaned spectrum is shown with dashed line.

E9156

with  $\alpha_0/n_M = 0.02 \text{ cm}^{-1} \mu\text{M}^{-1}$ ,  $\alpha_{\text{sat}}/n_M = 0.16 \text{ cm}^{-1} \mu\text{M}^{-1}$ ,  $J_{\text{sat}} = 1.28 \pm 0.02 \text{ mJ/cm}^2$ , and  $n = 1.50 \pm 0.04$ . For incident fluences higher than  $\sim 30 \text{ mJ/cm}^2$ , increased nonlinear absorption was observed instead of saturable absorption (decrease in transmission by 2%–3%). The operating incident intensity was chosen near 20 to 25  $\text{mJ/cm}^2$ . The measured transmission of the cell was  $\exp(-\alpha_0 L) = 22\%$  with a Kodak-dye concentration of  $\sim 75 \mu\text{M}$ , and the expected contrast boost was  $\exp(\alpha_{\text{sat}} L) \sim 10^5$ .

The autocorrelator was constructed as follows: A 10-mm  $\times$  10-mm, 4-mm-thick  $\text{LiIO}_3$  crystal with rms surface roughness below 50 Å and bulk index-of-refraction inhomogeneities below  $10^{-5} \text{ cm}^{-1}$  was chosen as the noncollinear crystal. The two beams had a crossing angle  $\Phi \approx 19^\circ$  ( $\sim 75^\circ$  in the air). Without a down-collimator and on-crystal focusing lenses, the autocorrelator was used to measure the pulse duration in a single shot. The diameter of each individual beam was  $2w_0 \sim 5.6 \text{ mm}$ . With a down-collimator before the saturable absorber cell and with the insertion of  $f = 125\text{-mm}$  lenses  $L_1$  and  $L_2$  (see Fig. 75.10), the two beams were focused onto the crystal with waist sizes of  $40 \mu\text{m}$ . The crystal was cut for type-I noncritical phase matching. An after-crystal slit with a width of  $d_{\text{sl}} \approx 300 \mu\text{m}$  was placed  $L_{\text{sl}} = 1 \text{ mm}$  behind the crystal, as shown in Fig. 75.9. The autocorrelator was carefully aligned with respect to any geometrical displacement of the probe beam inside the crystal when the translation stage is scanned. A photomultiplier tube (PMT), heavily filtered against the fundamental frequency and attenuated with variable-calibrated neutral-density filters to keep the signal on the same level, was used as the detector. The signal from the PMT was additionally time gated to avoid any noise associated with two-photon fluorescence, or any other long-time-scale optical noise. The signal from the PMT was an electrical pulse  $\sim 4 \text{ ns}$  in duration. This electrical pulse was integrated within the gate time of 80 ns and converted into counts. One count from our acquisition system corresponded to 4 optical photons. The combined optical and electrical noise level with the PMT exposed to the experimental surroundings, without attenuating neutral-density filters and without blocking the noncollinear signal, was 2 counts.

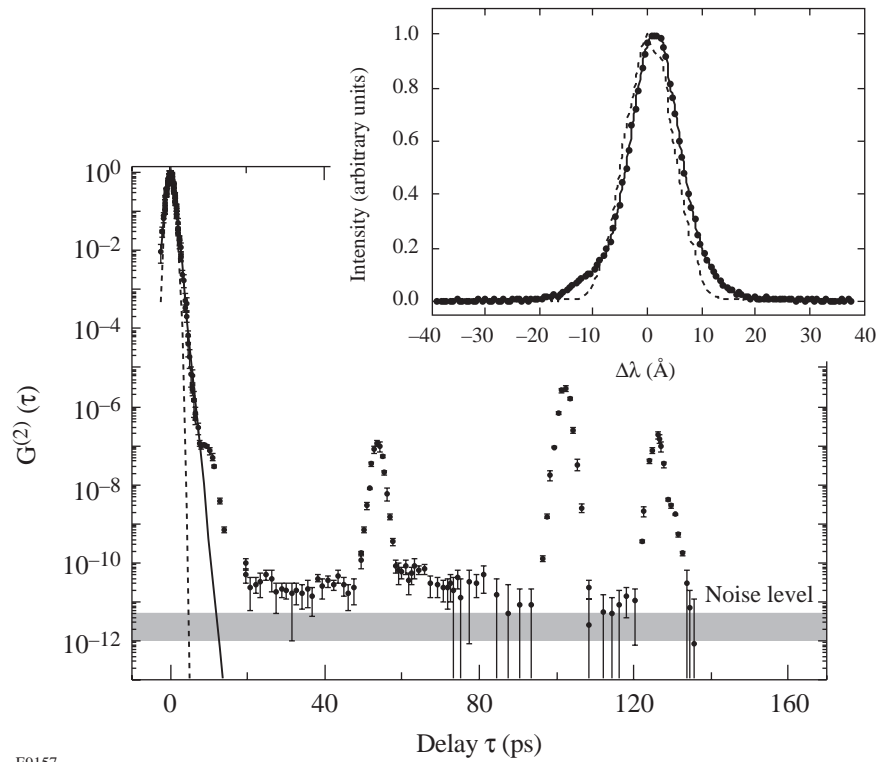
The second-order autocorrelation measurements of pulses cleaned with OPC and SA are shown in Fig. 75.13. Each point of the autocorrelation curve in Fig. 75.13 corresponds to an average of five laser shots. The inset shows the measured spectrum before and after the SA cell. From the spectral measurements, it can be seen that the  $B$ -integral accumulated in the SA cell is  $\sim 1$ . The estimated  $B$ -integral in the rest of the

autocorrelator optics is  $\sim 0.3$ . After transmission through the SA cell, the duration of the pulse was reduced from 1.4 ps to 1.0 ps. The peaks at 54, 100, and 125 ps are Fresnel reflections from optics in the autocorrelator. The pulse is measured to have an intensity contrast in excess of  $10^{11}$ .

The dynamic range of the autocorrelator, measured as the ratio of the peak of the signal to the sum of the signals measured from each arm while the other arm was blocked, was  $10^8$  without the after-crystal slit and  $10^{11}$  with it. Noise from each arm represented a constant addition to the signal, independent of the delay, but proportional to the square of the energy of the fundamental light at the input of the autocorrelator. That additional noise can be subtracted from the signal for each shot, leaving not the noise level from each arm, but rather the uncertainty of the noise level of each arm. The uncertainty of the noise level of each arm was 20% of the noise itself; thus, the system was able to resolve the signal with a dynamic range of  $0.5 \times 10^{12}$ . The signal at large delays was about twice as large as the noise.

The estimates based on the simple geometric layout shown in Fig. 75.9 with Gaussian beam profiles show that our approach can be applied to pulses as short as 100-fs duration. For pulses shorter than  $\sim 100 \text{ fs}$ , both the geometry and the phase-matching conditions over the 10-nm spectrum may make it difficult to reduce the surface-scattering noise, which may decrease the dynamic range of an autocorrelator. The shorter pulses require higher temporal resolution (smaller  $\Delta\tau$ ) and thus smaller crossing angles. Smaller crossing angles would require a longer crystal. Longer crystals would cause the distortion of the temporal shape of the pulse (due to material dispersion) before it reached the interaction region. Tighter focusing would bring noncollinear frequency conversion closer to saturation with lower energies of the crossing fundamental beams and would give smaller noncollinear beam energies. The after-crystal slit still might be a solution with 100- $\mu\text{m}$ -thick crystals and tighter focusing for multikilohertz systems able to generate  $\sim 30\text{-fs}$  pulses<sup>3</sup> because one can utilize lock-in detection.

In conclusion, we have demonstrated for the first time second-order autocorrelation measurements of ultrashort picosecond pulses with dynamic ranges of  $\sim 0.5 \times 10^{12}$ . To our knowledge, this is the highest dynamic range obtained in time-resolved dynamic-range measurements with tens-of-femtoseconds resolution. To our knowledge, this is also the first consideration of dynamic-range limitations for noncollinear, high-dynamic-range autocorrelation measurements.



E9157

Figure 75.13

Normalized second-order autocorrelation of the OPC-cleaned pulses (as shown in Fig. 75.11 with open diamonds) after transmission through the SA cell. A  $10^{-12}$  signal corresponds to  $\sim 4$  photons per shot. The final autocorrelation function has peaks at 54 ps, 100 ps, and 125 ps at a level of  $10^{-5}$  to  $10^{-6}$  below the peak intensity. These are Fresnel reflections in the autocorrelator optics and in the SA cell. The 54-ps peak is associated with the reflection from the 5-mm-thick non-wedged mirror ( $M_2$  in Fig. 75.10) in the translation-stage arm. It can be eliminated by using a wedged mirror. The 100-ps peak is the secondary reflection in the plano-convex ( $f=125$  mm, thickness = 10 mm) on-crystal focusing lenses ( $L_1$  and  $L_2$  in Fig. 75.10). This expected peak was at a different position when focusing lenses with a different thickness were used. It can be reduced and eliminated by better coating and with a slight misalignment of the focusing lenses. The 125-ps peak is the Fresnel reflection from the 1/2-in.-thick wall of the second SA cell. It disappeared but was replaced by a similar peak at 10 ps when a SA cell with 1-mm-thick walls was used. The inset shows the intensity spectrum of the pulses before (dashed line) and after (solid line) transmission through a SA cell for incident fluences of  $\sim 25$  mJ/cm<sup>2</sup>. After transmission through the cell, the pulse duration decreased from 1.4 ps to 1.0 ps. The dashed and solid curves are, respectively, 1.0-ps Gaussian and sech<sup>2</sup> fits to this autocorrelation data.

## ACKNOWLEDGMENT

This work was supported by the U.S. Department of Energy Office of Inertial Confinement Fusion under Cooperative Agreement No. DE-FC03-92SF19460, the University of Rochester, and the New York State Energy Research and Development Authority. The support of DOE does not constitute an endorsement by DOE of the views expressed in this article.

## REFERENCES

1. P. B. Corkum *et al.*, Phys. Rev. Lett. **61**, 2886 (1988).
2. B. C. Stuart *et al.*, Phys. Rev. B **53**, 1749 (1996).
3. A. Antonetti *et al.*, Appl. Phys. B **B65**, 197 (1997).
4. G. A. Mourou, C. P. J. Barty, and M. D. Perry, Phys. Today **51**, 22 (1998).
5. A. Galvanauskas *et al.*, Opt. Lett. **23**, 210 (1998).
6. I. N. Ross *et al.*, Opt. Commun. **144**, 125 (1997).
7. M. M. Murnane, H. C. Kapteyn, and R. W. Falcone, Phys. Rev. Lett. **62**, 155 (1989).
8. H. Chen, B. Soom, B. Yaakobi, S. Uchida, and D. D. Meyerhofer, Phys. Rev. Lett. **70**, 3431 (1993).
9. B. Soom, H. Chen, Y. Fisher, and D. D. Meyerhofer, J. Appl. Phys. **74**, 5372 (1993).
10. Throughout the text it is assumed that the contrast of some structure is the ratio of the peak intensity of the pulse to the intensity of this structure, while the intensity level of a structure is the inverse of the contrast.

11. M. Tabak *et al.*, Phys. Plasmas **1**, 1626 (1994).
12. E. P. Ippen and C. V. Shank, Appl. Phys. Lett. **27**, 488 (1975).
13. G. Albrecht, A. Antonetti, and G. Mourou, Opt. Commun. **40**, 59 (1981).
14. R. Wyatt and E. E. Marinero, Appl. Phys. **25**, 297 (1981).
15. P. Pax, J. Weston, and W. E. White, in *Femtosecond to Nanosecond High-Intensity Lasers and Applications*, edited by E. M. Campbell (SPIE, Bellingham, WA, 1990), Vol. 1229, pp. 82–86.
16. A.-C. Tien *et al.*, Opt. Lett. **22**, 1559 (1997).
17. R. Trebino and D. J. Kane, J. Opt. Soc. Am. A **10**, 1101 (1993).
18. J. Janszky, G. Corradi, and R. N. Gyuzalian, Opt. Commun. **23**, 293 (1977).
19. C. Kolmeder, W. Zinth, and W. Kaiser, Opt. Commun. **30**, 453 (1979).
20. K. Yamakawa *et al.*, Opt. Lett. **16**, 1593 (1991).
21. Y.-H. Chuang, D. D. Meyerhofer, S. Augst, H. Chen, J. Peatross, and S. Uchida, J. Opt. Soc. Am. B **8**, 1226 (1991).
22. L. Zhao *et al.*, in *Mode-Locked and Solid State Lasers, Amplifiers, and Applications*, edited by M. Piché and P. W. Pace (SPIE, Bellingham, WA, 1993), Vol. 2041, pp. 93–102.
23. D. M. Gold, Opt. Lett. **19**, 2006 (1994).
24. P. Beaud *et al.*, in *OSA Proceedings on Shortwavelength V: Physics with Intense Laser Pulses*, edited by M. D. Perry and P. B. Corkum (Optical Society of America, Washington, DC, 1993), Vol. 17, pp. 11–15.
25. O. A. Konoplev, Y. Fisher, and D. D. Meyerhofer, in *Conference on Lasers and Electro-Optics*, Vol. 15, 1995 OSA Technical Digest Series (Optical Society of America, Washington, DC, 1995), p. 216.
26. Y. Beaudoin *et al.*, Opt. Lett. **17**, 865 (1992).
27. R. S. Marjoribanks *et al.*, Opt. Lett. **18**, 361 (1993).
28. C. N. Danson *et al.*, Opt. Commun. **103**, 392 (1993).
29. C. Rouyer *et al.*, in *OSA Proceedings on Shortwavelength V: Physics with Intense Laser Pulses*, edited by M. D. Perry and P. B. Corkum (Optical Society of America, Washington, DC, 1993), Vol. 17, pp. 2–5.
30. M. P. Kalashnikov *et al.*, Phys. Rev. Lett. **73**, 260 (1994).
31. J. P. Chambaret *et al.*, Opt. Lett. **21**, 1921 (1996).
32. J.-L. Tapié and G. Mourou, Opt. Lett. **17**, 136 (1992).
33. P. F. Curley *et al.*, Opt. Commun. **120**, 71 (1995).
34. A. Braun *et al.*, Opt. Lett. **20**, 1889 (1995).
35. I. D. Jung *et al.*, Appl. Phys. B **B65**, 307 (1997).
36. K. Yamakawa *et al.*, IEEE J. Quantum Electron. **27**, 288 (1991).
37. C. Y. Chien, G. Korn, J. S. Coe, J. Squier, G. Mourou, and R. S. Craxton, Opt. Lett. **20**, 353 (1995).
38. Y. Wang and B. Luther-Davies, J. Opt. Soc. Am. B **11**, 1531 (1994).
39. L. L. Losev and V. I. Soskov, Opt. Commun. **135**, 71 (1997).
40. P. Heinz and A. Laubereau, J. Opt. Soc. Am. B **6**, 1574 (1989).
41. E. P. Ippen, and C. V. Shank, in *Ultrashort Light Pulses*, edited by S. L. Shapiro, Topics in Applied Physics, Vol. 18 (Springer-Verlag, Berlin, 1977), pp. 83–122.
42. S. Umegaki and S. Tanaka, Jpn. J. Appl. Phys. **16**, 775 (1977).
43. H. E. Bennett and J. O. Porteus, J. Opt. Soc. Am. **51**, 123 (1961).
44. D. A. Roberts, IEEE J. Quantum Electron. **28**, 2057 (1992).
45. L. D. Landau and E. M. Lifshitz, *Electrodynamics of Continuous Media*, Course of Theoretical Physics, Vol. 8 (Pergamon Press, Oxford, 1960), p. 385.
46. H. Bach and N. Neuroth, in *The Properties of Optical Glasses*, Schott Series on Glass and Glass Ceramics (Springer-Verlag, Berlin, 1995), p. 88.
47. P. Bado, M. Bouvier, and J. S. Coe, Opt. Lett. **12**, 319 (1987).
48. O. A. Konoplev and D. D. Meyerhofer, IEEE J. Sel. Top. Quantum Electron. **4**, 459 (1998).
49. R. H. Stolen, J. Botineau, and A. Ashkin, Opt. Lett. **7**, 512 (1982).
50. B. Nikolaus, D. Grischkowsky, and A. C. Balant, Opt. Lett. **8**, 189 (1983).
51. H. Roskos *et al.*, Opt. Commun. **61**, 81 (1987).
52. W. J. Tomlinson, R. H. Stolen, and A. M. Johnson, Opt. Lett. **10**, 457 (1985).
53. B. Kopainsky, W. Kaiser, and K. H. Drexhage, Opt. Commun. **32**, 451 (1980).
54. Y.-H. Chuang, J. Peatross, and D. D. Meyerhofer, in *Short-Pulse High-Intensity Lasers and Applications*, edited by H. A. Baldis (SPIE, Bellingham, WA, 1991), Vol. 1413, pp. 32–40.